Engineering of surface oxygen vacancies in Co-free concentration-gradient Li-rich cathodes for high-capacity batteries

P. Vahdatkhah [a, b], O. Voznyy [a, **], S.K. Sadrnezhaad [b, *]

[a] Department of Physical & Environmental Sciences, Department of Chemistry, University of Toronto, Toronto, ON, M1C 1A4, Canada
[b] Department of Materials Science and Engineering, Sharif University of Technology, 11365-9466, Tehran, Iran

ARTICLE INFO

ABSTRACT

Li-rich layered oxides (LLOs) are the most promising high-capacity materials in the Li-ion batteries owing to their cumulative oxygen anionic and cationic redox reactions. However, irreversible oxygen evolution and transition-metal migration aggravate structural rearrangement and capacity fading. Although Co-containing LLO possesses practical capacity and stability for commercial purposes, it suffers from scarcity, toxicity, and high cost of cobalt. To ameliorate these bottlenecks, we improved the reversibility of anionic and cationic redox in Co-free concentration-gradient LLO by integrating oxygen vacancies and high Ni/Mn ratio on LLO's surface. We found that surface oxygen vacancies suppress oxygen release from the surface, reduce the interfacial resistance that arises from electrolyte decomposition, and increase the ionic diffusion; thereby, enhancing the cathode's capacity. Concentration-gradient LLO cathode with an appropriate Mn/Ni ratio improved cation migration's structural stability and reversibility in the layered and spinel-layered Li-rich materials. As a result, the charge transfer and interfacial resistance decreased during the gradual de-lithiation and Ni redox reaction. The Co-free LLO with surface Mn/Ni~1.5 delivered a reversible capacity of 250 mAh/g, with 99% capacity retention after 85 cycles at 0.1 C. This work provided a practical approach for resolving the capacity decay of the Co-free LLOs by engineering the cathode/electrolyte interface and structure.

1. Introduction

Li-rich layered oxides (LLOs), x Li$_2$MnO$_3$·(1−x) LiMO$_2$ (M = Ni, Co, Mn), are considered promising high-capacity cathode materials (exceeding 250 mAh/g) for the near future high-energy-density Li-ion batteries. Compared to commercialized cathode materials such as LiCoO$_2$, LLO exhibits an anionic redox couple in addition to the usual transition metal (TM) redox couples [1]. The activation of the Li$_2$MnO$_3$ phase in LLO materials above 4.5 V leads to the extraction of Li$^+$ from the Li and TM layers along with oxygen anionic redox, thereby providing extra capacity [2].

The anionic redox mechanism has proved challenging; however, a clear consensus has been reached that it involves two contributions: a reversible oxygen redox within the bulk structure and an irreversible oxygen evolution on the surface, which resulted in a reduction of oxygen redox activity [3–6]. There are two theories that can explain the oxygen redox and irreversible oxygen loss based on the complication of the oxygen redox mechanism in 3d TM LLOs [6]. The first theory is based on the formation of peroxo-oxygen dimers (O$^-$–O$^-$) and reversible oxygen redox stems from O^{2-}/O$^-$ redox process [7]. The studies find that these dimers across the LLO surface are highly active, and O$_2$ and/or CO$_2$ evolution can occur by them reacting together and/or with electrolyte, respectively [8].

The second theory states that anionic redox is based on the formation of oxygen holes [6]. Some claim that localized electron holes were created during charging in the O2p orbitals of O−(Mn^{4+}/Li$^+$) bonds, which are less covalent than O−Ni^{4+} bonds. Therefore, the release of O from the lattice can occur due to instability of oxidized O^{2-} species [9]. While others indicate that oxygen holes along the Li−O−Li configuration join together and form peroxo-like species, leading to oxygen oxidation. They found that when electrons were extracted from the unhybridized oxygen orbital, two neighboring oxidized oxygens rotated to hybridize, without sacrificing much transition metal−O hybridization,

* Corresponding author.
** Corresponding author.
 E-mail addresses: o.voznyy@utoronto.ca (O. Voznyy), sadrnezh@sharif.edu (S.K. Sadrnezhaad).

therefore O−O bond is formed [10]. However, the neighboring oxidized oxygen ions, in particular, surface oxygens were difficult to rotate and to form a stable O−O bond, thereby leading to oxygen loss [11]. Besides, these holes generally cause the reduction of TM-O bonding strength, and result in oxygen release [6].

Another pernicious problem of LLO involves the irreversible cation migration from the TM layer to Li layer during the delithiation process, which is exacerbated by oxygen redox. The released oxygen causes the generation of some oxygen vacancies on the surface/sub-surface and assists the TM migration [12]. This TM migration results in the formation of a spinel-like phase [5,13,14], TM dissolution into the electrolyte at high voltage [15], and hence, rapid electrode degradation in terms of capacity and stability.

Until now, most research efforts have been dedicated to the control of oxygen gas release [12,16] or the cation migration in LLO [13], although they affect each other [5]. On the one hand, to reduce oxygen release and utilize reversible anionic redox activity over cycling, surface sulfur polyanions [17,18], disordered rocksalt [19], and surface oxygen vacancies using gas-solid interface reaction [12], reducing atmosphere [20,21], solid electrolyte reactor composed of a Yttria Stabilized Zirconia tube [22], leaching with acid [23,24], and mixing with ammonium bicarbonate [25] have also been proposed.

On the other hand, various strategies focusing on compositional tuning [26], structure designing [13,27−29], surface modifications [30−34], cation and anion doping [30,35−37], and electrolyte composition [38,39] have been developed to alleviate the complex cation migration in LLO during cycling.

In addition to the methods mentioned above, recently, LLO cathodes with a concentration-gradient (LLO-CG) structure exhibited improved performance, including highly reversible capacity and thermal stability [16,40−42]. As such, LLO-CG is more mechanically stable compared to core-shell structures due to decreasing mismatch-induced strain [40]. So far, a few LLO-CG structures were reported, such as particles with a Li-rich interior and a Li-poor surface by a molten salt treatment [16], Li-rich nickel cobalt manganese oxides cathode with gradient distributions of TM ions by using ethanol assisted, and PO_4^{3-}-doping co-precipitation method, respectively [41,42]. Besides, the surface with a high Ni/Mn ratio promotes the capacity and suppresses side-reactions on the electrode/electrolyte interface due to reduced Li_2MnO_3 with poor conductivity and O_2 evolution. Moreover, more Ni with higher reduction potential provides higher working voltage. Controlling the gradient distribution of TMs in the LLO cathode is significant; however, the different ratio of TMs on the electrochemical properties of the cathode is still not fully understood.

Therefore, although various effective approaches have been used to improve the reversibility of either anionic or cationic redox, it is crucial to control both reactions because suppressing the oxygen evolution cannot prevent the cation migration to the vacant Li sites, which originates from the deintercalation of Li ions [13], and vice versa. Nevertheless, up to date, minimizing the capacity decay while using combined cationic and anionic redox has not yet been achieved. This is due to the difficulty of doing so in conventional synthesis methods, e.g., co-precipitation as it needs multi-step complicated treatments to engineer both the structure and surface of the cathode, and consequently, the high cost for scalable industrial applications. Apart from performance, Co-containing LLO materials suffer from cobalt's low availability, high cost, and toxicity, though they possess practical capacities and stability for commercial purpose [43].

Inspired by the considerations above, the preparation of Co-free LLO-CG with surface oxygen vacancies and suitable composition via polyol-mediated process and subsequent calcination-driven diffu-

sion route is a novel and more effective method to control the capacity loss of the LLO materials, which has not yet been explored. We apply a new surfactant-assisted polyol synthesis to obtain a series of Li(Na-doped)-Mn-Ni-O oxide systems with a concentration gradient of TM ions by controlling the calcination time/temperature, type, and amount of surfactant as well as reducing agent.

Without the need for careful control of pH or an inert atmosphere, the proposed polyol method offers the benefits of low cost, simplicity, versatility, scalability for large-scale applications, and producing monodispersed nanoparticles morphology, which is desirable for surface and interface studies [44]. In this process, polyol acts as a solvent, reducing, chelating, and stabilizing agent to prevent nanoparticle aggregation. Moreover, shape, size, and component can be manipulated by affecting various factors such as polyol type, reducing agent, capping agent, and reagent concentrations [44,45].

Herein, we demonstrate that the composition and Mn/Ni ratio can be tuned by changing the type and amount of reducing agent. Based on the electrochemical results, the suitable Mn/Ni ratio for reaching high capacity was obtained in CG-LLO and spinel/LLO structures. In addition, the carbon-based solvent (ethylene glycol) and reducing agent (urea) produced the reducing environment to create surface oxygen vacancies. As a result, the Co-free LLO material with surface oxygen vacancies, and Mn/Ni~1.5 delivers a capacity as high as 254 mAh/g, with 99% capacity remaining after 85 cycles at 0.1C.

2. Methods

2.1. Synthesis of $Li_xMn_yNi_zO_2$ (LMNO = LLO and LLO/Spinel) materials

Synthesis of precursor (manganese nickel hydroxide or carbonate): TM chlorides- $NiCl_2.6H_2O$ (0.0017 mol) and $MnCl_2 \cdot 4H_2O$ (0.005 mol)- were mixed in 20 mL of ethylene glycol (EG) along with surfactant (cetyltrimethylammonium bromide (CTAB)-oleylamine) and reducing agent (NaOH−LiOH-urea). The mixture was heated at 180 °C with constant stirring for 20 h in a round bottom flask connected to reflux. The resulting solution was washed with ethanol and deionized water several times with a centrifuge and dried at 80 °C overnight.

Final step, synthesis of LMNO material: as-obtained precursors were decomposed at 500 °C for 6 h. The as-prepared TM oxide precursor was thoroughly mixed with different amounts of $LiOH.H_2O$ in an agate mortar and annealed at different calcination temperatures (700−900 °C) and times (8−16 h) in air.

2.2. Database

In this study, a total number of eight experiments for LMNO cathodes, whose Li content is between 0.525 and 1.2 stoichiometric content of $Li_{1.2}Ni_{0.2}Mn_{0.6}O_2$, were constructed with 6 input principal variables of synthesis parameters (LiOH.H2O amount, type and amount of reducing agent, type of surfactant, and calcination temperature and time). The parameters were selected using a random uniform distribution within the given ranges, (https://sigopt.com/), with a goal of using this set as a seed for future more detailed parameter space studies.

Previous results showed that $0.5Li_2MnO_3 \cdot 0.5LiMn_{0.5}Ni_{0.5}O_2$ ($Li_{1.2}Mn_{0.6}Ni_{0.2}O_2$) could deliver a high discharge capacity of ~240 mAh/g between 2.0 and 4.8 V[46]. Then, the stochiometric amounts of Mn−Ni were used from the formula $Li_xNi_{0.2}Mn_{0.6}O_y$ oxide system, with a wide range of Li content (x: between 0.525 and 1.2 of the stoichiometric value with 10% excess amount) to

compensate Li loss because of the evaporation of Li at high temperature. The Li concentration in the synthesized compounds was also somewhat changed by adding LiOH reducing agent. Nevertheless, the amount of Li decrease in the final calcination is not equal in all samples because of different calcination temperatures/time, reducing agents, and Li_2CO_3 formation on the surface of samples. The prepared materials were, respectively, marked as L0.525, …, L1.2 (Table 1).

In this study, three types of reducing agents (NaOH, LiOH, and urea) were used in the polyol process for reducing the transition metals. It has been shown that the type of reducing agent and its concentration play a significant role in the reduction rate of the transition metal ions [47], as well as the size and morphology of the obtained precipitates [48]. With an increase of reducing agent concentration, the reduction rate of ions, and number of nuclei enhances, thereby smaller particles can be achieved [47]. Furthermore, LiOH is a weaker reducing agent than NaOH, which led to a slower reduction process [49]. Besides, the morphology can be adjusted by changing the reducing agent. In previous studies, nanosheets and nanoparticles have been obtained using NaOH and LiOH, respectively, due to the smaller ionic radius of Li ions than Na [48]. Additionally, urea releases CO_3^{2-} instead of OH^- for the precipitation of the transition metal ions [50]; therefore, it affects the amount of carbonate/carbon and the finally generated oxygen vacancy.

Moreover, it has been reported that various spinel/layered structures with different electrochemical performance can be obtained by changing the calcination temperature from 500 to 900 °C [51]. Besides, the change in calcination time was studied to investigate the synthesis process (8-12-16 h). Meanwhile, the effect of surfactants (CTAB [52] and oleylamine [53]) on the morphology, chemical composition and structure, and particle size was studied by controlling the particle growth.

2.3. Characterization

X-ray diffraction (XRD) and X-ray photoelectron spectroscopy (XPS) patterns for cathode materials were recorded using Rigaku-Miniflex-6G diffractometer and Thermo Scientific K-Alpha to identify the crystallography phase and surface chemical composition, respectively. Inductively coupled plasma- optical emission spectroscopy (ICP-OES) was carried out on Axial ICP-OES, Varian. 730-ES, to investigate the elemental analysis of the oxide samples. The microstructure, morphology, and particle size of the specimens were characterized by field emission scanning electron microscope (FE-SEM, MIRA3 TESCAN). Infrared spectra (4000−400 cm^{-1}) of solid samples were taken as a 1% dispersion in KBr pellets using a Unicam Matson 1000 Fourier-transform infrared spectroscopy (FTIR) spectrophotometer.

The electrochemical performance of the prepared cathodes was investigated by galvanostatic cycling in a coin-type half-cell (CR2032). The coin cells were assembled in an argon-filled glove box (LC Technology Solutions, INC.), with lithium metal (15.6 mm diameter, 250 μm thickness) as the anode, 100−200 μL electrolyte (1 M $LiPF_6$ in EC/DMC = 1:1 in volume, BASF), and Celgard 2400 membrane as the separator. The cyclic voltammetry (CV) and electrochemical impedance spectroscopy (EIS) measurements of the coin cells were conducted using a VMP3 multi-channel potentiostat (Bio-Logic, France). Further details on the synthesis procedure, database, and characterization techniques can be found in the Supplementary Methods. The first-principles calculations were performed with the spin-polarized density functional theory (DFT) calculations using CP2K. Further details on the synthesis procedure, database, and characterization techniques can be found in the Supplementary Methods.

3. Results

3.1. Synthesis mechanism

Synthesis of LMNO materials is a two-step process that involves: 1) preparation of the precursors via polyol solution reaction and 2) mixing the precursor with Li hydroxide and heat-treatment to complete the phase transformation and eliminate impurities (Fig. 1). So, a series of Na-doped Li−Mn−Ni−O oxide systems with different contents of Li-TM cations were obtained by adding different amounts of lithium source into a resulting precursor from the polyol process.

The polyol process consists of two steps: 1) forming metal complexes and 2) hydrolysis/condensation of metal chelates [45]. The complexation of metal ions would occur with chloride ions and ethylene glycol. The hydroxide salts (NaOH, LiOH) or urea solutions become hydroxide or carbonate groups, respectively, according to Eq. (1). Then, the substitution of these groups occurs with chloride ions and TM hydroxide or carbonate forms. After polyol synthesis, there is a different Mn/Ni ratio in the precursor by using different reducing agents; see chemical composition analysis of selected samples (Table 1).

When the reducing agent was added to the solution composed of chloride salts and EG, the color of the solution turned from light green (neon) to dark green (sacramento), dark yellow, and finally black in the case of urea (e.g., L1.00); as well as brown (at room temperature) and lime (at higher temperatures close to boiling point) in the case of NaOH and LiOH (e.g., L0.525 and L0.625), respectively. Simultaneous use of CTAB and NaOH leads to forming the sage color solution (e.g., L0.825).

Afterward, the transition metal oxide can be formed by calcination of hydroxide/carbonate precursor (Eqs. (2) and (3)). During this process, some of EG and its deprotonated molecules can be transformed to carbon by releasing CO_2 and H_2O. In the final step, after Mn_xNiO_4 mixing with LiOH, followed by calcination, $Li_z(Mn_xNi)_yO_2$ and Li_2CO_3 products were obtained according to Eqs. (4) and (5).

Table 1
Selected LMNO cathodes from the dataset, ICP, XPS, and XRD results.

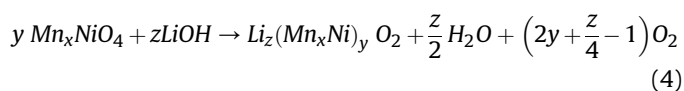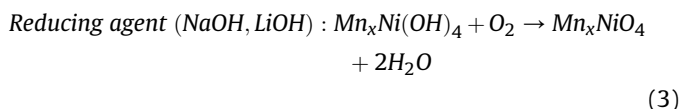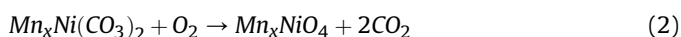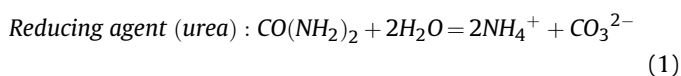| Sample No.	LiOH/$NiCl_2$ molar ratio	Reducing agent	Surfactant	Calcination temp.	Calcination time	Mn/Ni ICP	Mn/Ni XPS	I(003)/I(104) XRD
L0.525-N-900	3.465	NaOH/TM = 1.8	Oleylamine	900 °C	16 h	3.22	1.2	2.46
L0.575-U-750	3.795	Urea/TM = 1.9	CTAB	750 °C	8 h	4.84	2.37	1.23
L0.625-L-750	4.125	LiOH/TM = 1.7	CTAB	750 °C	16 h	6.24	3.16	6.28
L0.825-N-750	5.445	NaOH/TM = 1.9	CTAB	750 °C	8 h	2.85	1.24	2.04
L0.925-L-700	6.105	LiOH/TM = 1.8	CTAB	700 °C	12 h	3.44	2.13	1.11
L1.00-U-850	6.6	Urea/TM = 1.6	CTAB	850 °C	16 h	1.95	1.44	1.06
L1.075-L-800	7.095	LiOH/TM = 1.8	Oleylamine	800 °C	8 h	3.44	2.08	1.77
L1.20-L-700	7.92	LiOH/TM = 2	CTAB	700 °C	16 h	2.31	−	
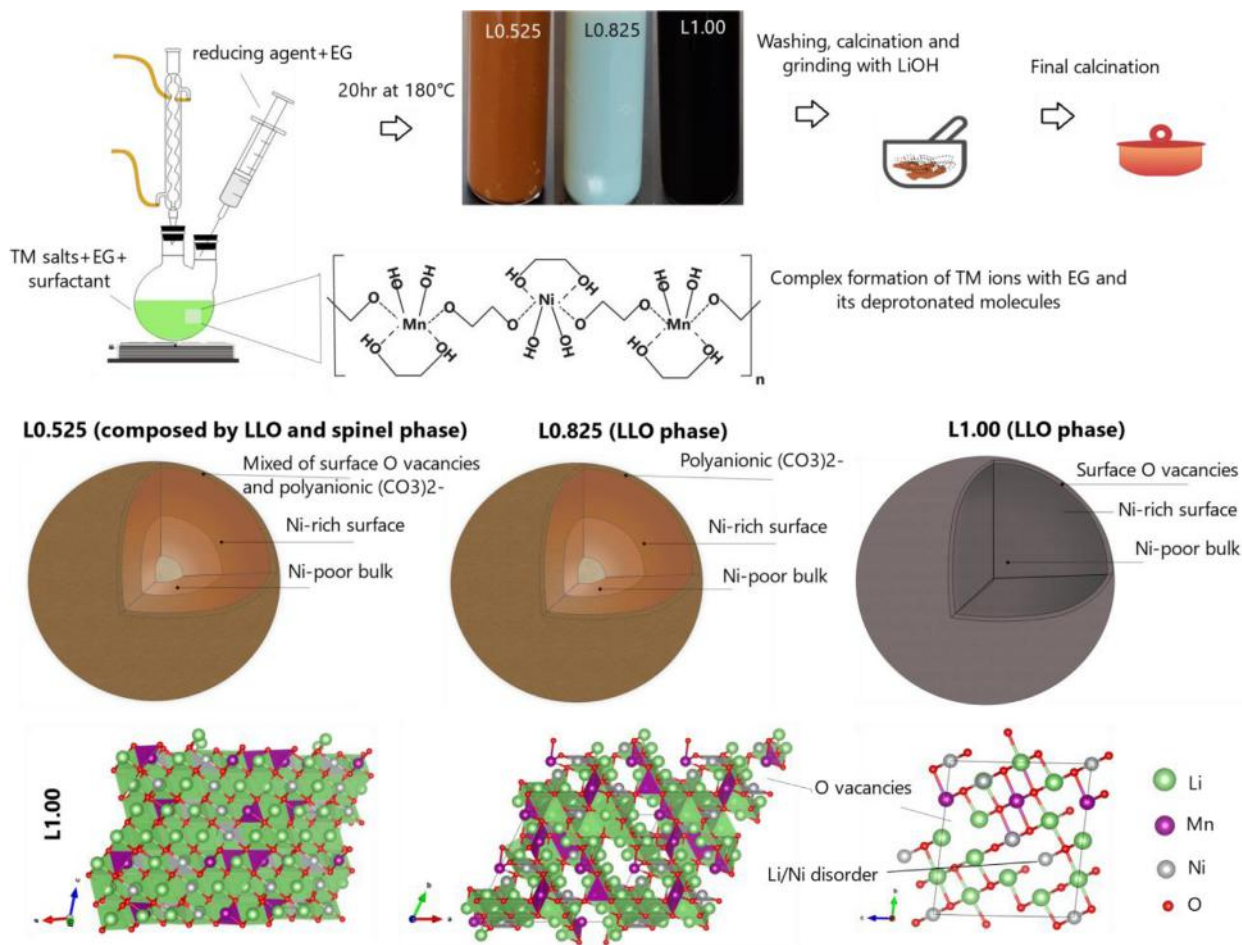
Fig. 1. Schematic of polyol-assisted method to synthesize Li−Mn−Ni−O oxides, reaction mechanism during synthesis, modification of LMNO samples by the creation of surface oxygen vacancies and/or polyanionic with a Ni concentration-gradient structure (L0.525 and L0.825), and surface oxygen vacancies with a uniform higher Ni content and Li/Ni cation mixing (L1.00).

$$Reducing\ agent\ (urea): CO(NH_2)_2 + 2H_2O = 2NH_4^+ + CO_3^{2-} \tag{1}$$

$$Mn_xNi(CO_3)_2 + O_2 \rightarrow Mn_xNiO_4 + 2CO_2 \tag{2}$$

$$Reducing\ agent\ (NaOH, LiOH): Mn_xNi(OH)_4 + O_2 \rightarrow Mn_xNiO_4 + 2H_2O \tag{3}$$

$$y\ Mn_xNiO_4 + zLiOH \rightarrow Li_z(Mn_xNi)_y\ O_2 + \frac{z}{2}H_2O + \left(2y + \frac{z}{4} - 1\right)O_2 \tag{4}$$

$$2LiOH + C + O_2 \rightarrow Li_2CO_3 + H_2O \tag{5}$$
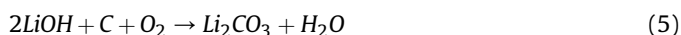
3.2. Material characterizations

3.2.1. Morphology of LMNO structures

Fig. 2 shows FE-SEM images for the TM oxide precursors and final products of L0.525, L0.825, and L1.00. Based on the optimal electrochemical performance of the cathodes and since a significant stepwise capacity increasing over cycling is observed in L0.525, L0.825, and L1.00, the characterization of these samples was studied in detail. The obtained precursor for L0.525 has the mesoscopic structure consisting of primary nanoparticles with size ~50 nm. Under calcining the polyol-derived precipitates, the self-assembly of nanoparticles into a mesostructure occurs in order to decrease the interfacial energy between the nanoparticles [28]. Moreover, the growth of nanocrystals is controlled by the low surface energies of planes [54], which are marked by arrows in Fig. 2a,c. The final L0.525 product has a polyhedral characteristic with sharp edges. Likewise, the L0.825 precursor shows aggregated nanoparticles (~25 nm) and less growth of nanocrystal planes compared with the L0.525 precursor due to the changing of surfactant from oleylamine to CTAB. The final L0.825 product (Fig. 2h) exhibits mesoscopic structural features by growth and assembly of the nanoparticles, which are favorable to reduce charge transfer resistance in the electrode/electrolyte interface and increase the ionic and electronic conductivity.

Interestingly, after the urea and CTAB treatment, the L1.00 precursor (Fig. 2i−k) shows uniform hierarchical hollow spheres, composed of primary nanoparticles with size ~35 nm. The driving force for the formation of hollow structure is the release of O_2/CO_2 gas volatilities from the interior of spheres [55]. With increasing the calcination temperature during the lithiation process, the final L1.00 product appears to have mesostructured morphology. The hollow structure of precursor leads to the formation of cavities on
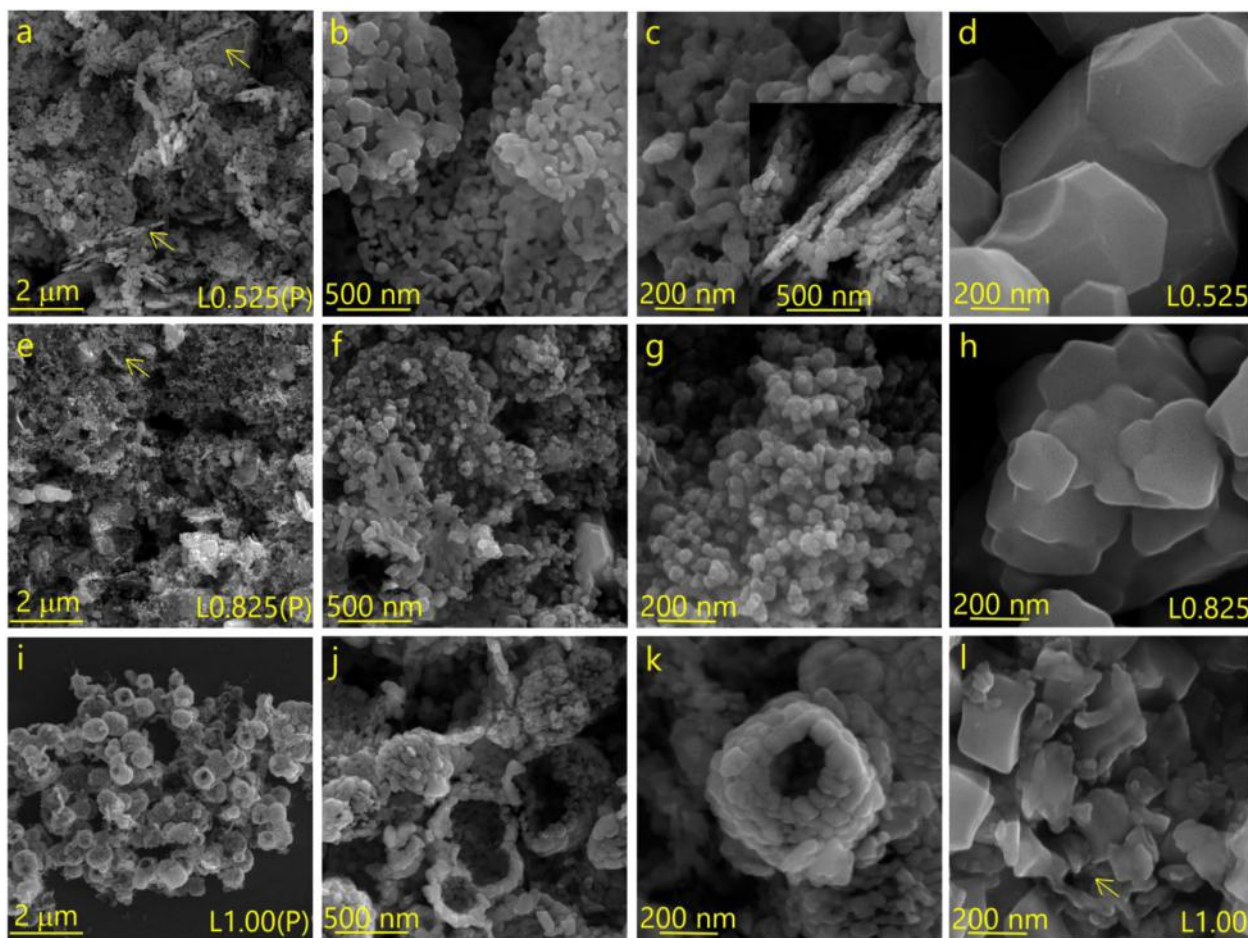
Fig. 2. FESEM images of the as-prepared TM oxide precursor of (a–c) L0.525 sample (denoted as L0.525(P)), (e–g) L0.825(P), and (i–k) L1.00(P), and final product of (d) L0.525, (h) L0.825, and (l) L1.00.

the final product, which is marked by arrow in Fig. 2l. Additionally, the EDS elemental mapping results for precursors and the final products of electrodes are shown in Figs. S1—S6, indicating a uniform distribution of each element in the samples.

3.2.2. Structural and chemical characterization of the LMNO products

As shown in Fig. 3a, XRD characterization was carried out to investigate the crystal structure of the L0.525 to L1.075 products. LLO exhibits the characteristics of the layered α-NaFeO$_2$ structure with the combined pattern of Li$_2$MnO$_3$ (space group: $C2/m$) and LiTMO$_2$ phase (space group: $R3m$, TM: transition metal). Notably, the spinel LiMn$_{1.5}$Ni$_{0.5}$O$_4$ phase (space group: 3Fdm) represents a slight shift of diffraction peaks, especially in the range of $36°-38°$ and $44°-45°$, as compared to LLO. From L0.525 to L0.625, the patterns of all the products suggest a composite of the layered and spinel phases. With the increasing Li content from L0.525 to L0.625, the spinel phase decreases, and the completely 'layered' structures could be observed in the XRD patterns of L0.825-L1.075 electrodes (see Supplementary Note1 for details).

Table 2 shows the chemical composition of the L0.525, L0.825, and L1.00 cathodes measured by ICP and EDX. According to the results, L0.525 and L0.825 materials form Na-doped Li-rich structures. LMNO structure receives more Li ions from LiOH salt, and the amount of Li$_2$CO$_3$ also increases. Except for L0.825 sample due to lower calcination temperature and reduction of CO$_2$ production. FTIR measurement was used to investigate the lithium carbonate formation on the LMNO surface (Fig. S7), in which the sharp

characteristic peaks located around 869, 1643, and 1500 cm^{-1} are attributed to the Li$_2$CO$_3$[43]. Besides, before transition metal oxide grinding with LiOH, there is some wastage of transition metal precipitation during washing, drying, and calcination steps; thus, the final Mn and Ni content is also lower than their stoichiometric amounts and leads to an increase in the stoichiometric lithium ratio in the final material.

3.2.3. Evaluation of concentration-gradient structures in LMNO cathodes

The surface and bulk chemical composition of products determined using XPS and ICP analysis, respectively, is shown in Fig. 3b. Since the depth of analysis for XPS measurement is ~5 nm, the XPS result can be attributed to surface composition of material. The decreased ratio of Mn/Ni on the surface compared with the bulk compositions indicates that concentration gradient LMNO cathodes were generated because Ni^{2+} has higher solubility constant value ($K_{sp} = 1.4 \times 10^{-7}$) than Mn^{2+} ($K_{sp} = 8.8 \times 10^{-11}$) and harder to precipitate [50]. Therefore, a concentration gradient can be formed in the precursors and final LMNO materials, as illustrated in Fig. 1.

Type and amount of reducing agent play a vital role in Mn/Ni ratio in the bulk and, subsequently, on the surface of LMNO. Weak (urea) and strong (LiOH, NaOH) bases have a different behavior in reducing the transition metals. The order of their reducing strength is NaOH > LiOH > urea. With increasing the base strength, more Ni can be precipitated along with Mn ions, thus there is a lower Mn/Ni ratio for L0.825 and L0.525 materials with NaOH/TM = 1.9 and 1.8,
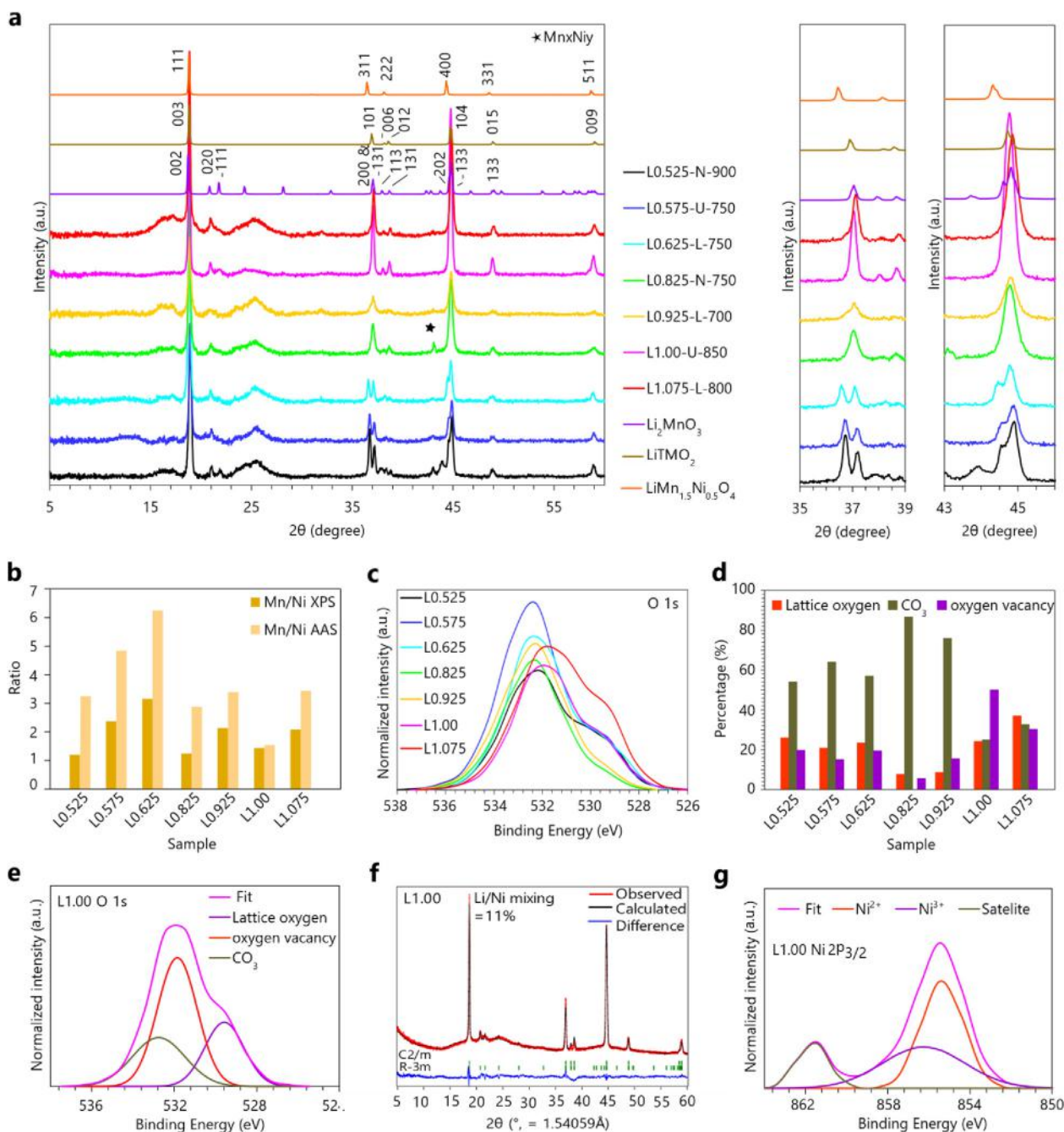
Fig. 3. Structural and chemical characterization of LMNO cathodes. (a) XRD patterns of the synthesized products with an amplified region of 35°−39° and 43°−46°. The standard Bragg position of Li_2MnO_3, $LiMn_{1.5}Ni_{0.5}O_4$, and $LiMO_2$ phases are indicated. The peak marked by rhombuses is the reflections originating from the Mn_xNi_y phase. (b) Ratio-stacked bar chart of surface and bulk Mn/Ni measured by XPS and ICP, respectively, (c) XPS of O 1s for all samples, (d) Percentage-stacked bar chart of oxygen species measured by XPS, (e) high-resolution O 1s for L1.00, (f) Rietveld refinement of L1.00, and (g) Ni2p spectra for L1.00.

respectively. However, the lowest Mn/Ni ratio was observed for L1.00 by using less urea, which shows the simultaneous tendency of Mn and Ni ions to precipitate, unlike faster precipitation of Mn ions in strong bases.

3.2.4. Evaluation of oxygen vacancies creation

The oxidation states of oxygen on the surface of all samples were determined by XPS after normalization of C 1s. The intensity of the binding energy at 529.46−529.77 eV representing TM-O covalency

Table 2
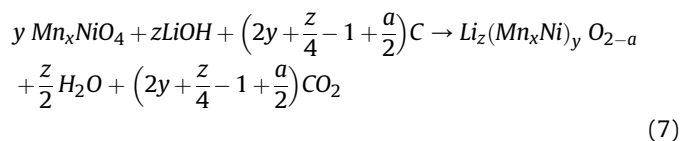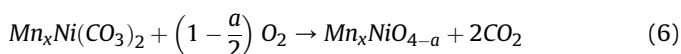Chemical composition of selected LMNO cathodes measured by ICP and EDX.

Sample No.	Chemical composition
L0.525	$(Li_{1.082} Na_{0.005}) Mn_{0.812}Ni_{0.252}O_{2.135}C_{0.025} = 1.03$ [**$(Li_{1.006} Na_{0.005}) Mn_{0.792}Ni_{0.246}O_2$**] $+0.025$ Li_2CO_3
L0.825	$(Li_{1.327} Na_{0.038}) Mn_{0.639}Ni_{0.225}O_{2.34}C_{0.1} = 1.01$ [**$(Li_{1.111} Na_{0.038}) Mn_{0.630}Ni_{0.221}O_2$**] $+ 0.1$ Li_2CO_3
L1.00	$Li_{1.44}Mn_{0.63}Ni_{0.32}O_{2.45}C_{0.055} = 1.14$ [**$Li_{1.17}Mn_{0.55}Ni_{0.28}O_2$**] $+ 0.055$ Li_2CO_3

is lower than that of the oxygen vacancy (531.29−531.93 eV) and the carbonate group ($-CO_3^{x-}$ at 532.47−532.85 eV) for almost all samples (Fig. 3c and d). This result is more clearly observed by the significant change on the intensity of the binding energy at 531.5 eV (Fig. 3e), which represents peroxo-like oxygen component O^{2n-}, that can be assigned to oxygen vacancies in the crystal lattice for the L1.00[3,12].

The creation of oxygen vacancies might be through two paths.

1) The ethylene glycol on the surface of precursors converts to carbon during calcination process.
2) Decomposition of urea leads to release the carbonate (CO_3^{2-}) at elevated temperature of polyol process (180 °C) through reaction 1 and thus the precipitation of carbonate precursor can be happened [50].

Therefore, according to Eqs. (6) and (7), some of surface lattice oxygens were released by CO_2 from carbonate and/or oxidation of carbon in the calcination step, forming oxygen vacancies on the LMNO surfaces, and using of urea promotes the creation of surface oxygen vacancies. By comparison of L0.575 and L1.00, it is worth noting that other conditions such as appropriate temperature along with urea is needed to have high oxygen vacancies.

$$Mn_xNi(CO_3)_2 + \left(1 - \frac{a}{2}\right) O_2 \rightarrow Mn_xNiO_{4-a} + 2CO_2 \tag{6}$$

$$y\,Mn_xNiO_4 + zLiOH + \left(2y + \frac{z}{4} - 1 + \frac{a}{2}\right)C \rightarrow Li_z(Mn_xNi)_y\,O_{2-a}$$
$$+ \frac{z}{2} H_2O + \left(2y + \frac{z}{4} - 1 + \frac{a}{2}\right)CO_2 \tag{7}$$

3.2.5. Li⁺/Ni²⁺ mixing

The intensity ratio of I(003)/I(104) < 1.2 is an indication of undesirable Ni^{2+}/Li^+ cation mixing; however, in some studies, it is observed that cation mixing improves the structural stability [56−59]. As summarized in Table 1, L1.00 shows higher cation mixing and disordered structure resulting from the high Ni content. Rietveld refinement of the XRD patterns was performed on the L1.00 sample (Fig. 3f and Table S1). The exact phases for L1.00 are $(Li_{0.882}Ni_{0.118})(Li_{0.118}Ni_{0.381}Mn_{0.5})O_2$ (70.9%) and $Li_{1.33}Mn_{0.67}O_2$ (29.1%) with refined Ni^{2+}/Li^+ mixing of 11%, corresponding to the composition of $Li_{1.17}Mn_{0.55}Ni_{0.31}O_2$, which is consistent with ICP results.

The oxidation states of TM on the surface of all samples were also measured by XPS. As observed in Fig. 3g and Fig. S9, the main peak for L1.00 is related to Ni^{2+}, manifesting the content of Ni^{2+} is higher than other samples. Thus, the higher Ni^{2+} content in L1.00 and cation mixing of Ni^{2+} in Li^+ sites is largely related to the two most important factors: increasing Ni content in the material and oxygen vacancy generation, leading to migration of the surrounding Ni ions in Li layers due to higher oxygen release. Furthermore, the ammonia from the decomposition of urea reduces the oxidation state of transition elements to compensate the unbalanced charge caused by the lattice oxygen deficiency [60]. The XPS spectra and fitted curves of O 1s, Na 1s, Mn 2p, and Ni 2p3/2 have been also shown in Figs. S8−S11 and Table S2 (see Supplementary Note2 for details).

3.3. Electrochemical performance

Galvanostatic charge−discharge measurements were carried out for a series of samples (L0.525-L1.2) at room temperature

(Fig. 4a and Fig. S12). There is a drastic evolution of the first charging voltage profile over much longer cycles in L0.525, L0.825, L1.00, and L1.075 samples upon diffusion of Ni on their surfaces (as discussed in the XPS results part). The surface Mn/Ni ratio around 2 was significant in stepwise capacity increase which leads to a higher lithium diffusion barrier near the surface region [61].

L0.525 shows the initial charge and discharge capacity of 99 and 93 mAh/g at 0.1C, which increases to 152 mAh/g after 150 cycles at 0.2C (Fig. 4a). To further support the electrochemical performance of cathodes, selected charge-discharge curves of the L0.525, L0.825, L1.00 and other cathodes at 0.1C are displayed in Fig. 4b−d and Fig. S13, respectively. Sample L0.525 (Fig. 4b), like L0.575 and L0.625 (as shown in Fig. S13), possesses a typical LLO-spinel composite structure, in which the wide plateau at about 4.5−4.8 V and the small plateau at 2.9 V during the charge process witness the existence of LLO and spinel phase, respectively. The discharge capacity of L0.525 increases to 205 mAh/g after 183 cycles at 0.1C. This increased capacity over cycling is attributed to a higher slant curve from 4.1 to 2.8 V associated to Ni redox.

L0.575 delivers the initial charge and discharge capacity of 389 and 261 mAh/g at 0.1C. After 150 cycles, the discharge capacity decays to 59 mAh/g at 0.2C (Fig. 4a). The increased initial charge capacity, compared to L0.525 electrode, is mainly ascribed to the wide plateau at 4.5−4.8 V, referring to the high Li_2MnO_3 content, its activation process and removal of Li ions accompanying oxygen evolution from it. Based on elemental analysis, the high Li_2MnO_3 is ascribed to high Mn amounts. XRD and electrochemical results exhibit that L0.575 has a layered-spinel phase in which the layered phase is higher than the spinel phase. Although L0.575 can deliver high initial capacity compared to L0.525, the irreversible capacity loss caused by extra removal of Li ions in first cycles leads to low capacity upon cycling.

The initial charge and discharge capacity of L0.625 are 316 and 209 mAh/g; the decreased discharge capacity in first cycle is ascribed to irreversible Li_2MnO_3 activation process. Sample of L0.625 have about 20% higher discharge capacities in the fifth cycle (253 mAh/g) than that in its first cycle, which is attributed to the suppressed Li_2MnO_3 activation process affected by the formation of a small amount of spinel phase on the surface [51]. L0.625 presents shorter plateau above 4.5 V, compared to L0.575, owing to more surface oxygen vacancies. L0.525 shows lower capacity in first cycles compared with L0.575 and L0.625 electrodes, but has a better stability upon long-term cycling, which is related to optimum Mn/Ni ratio on its surface.

Likewise, L0.825 with initial charge and discharge capacity of 312 and 146 mAh/g has a similar charge-discharge trend to L0.525 sample with maximum discharge capacity of 160.6 mAh/g after 104 cycles at 0.2C (Fig. 4a). Furthermore, the discharge capacity of L0.825 at 0.1C reaches to 172 mAh/g after 94 cycles (Fig. 4c). The reversible capacity retention ratio after 150 cycles relative to maximum discharge capacity at 0.2C and 0.1C is 98% and 92%, respectively.

However, L0.925, as a layered structure, demonstrates an initial charge and discharge capacity of 279.3 and 145.4 mAh/g at 0.1C, respectively; while the fourth discharge capacity is 178.8 mAh/g at 0.1C, which is related to gradual Ni redox (Fig. 4a). However, the capacity of L0.925 declines substantially after five cycles, and the material has 28 mAh/g after 150 cycles at 0.2C because of its low crystallinity as a result of low calcination temperature. The reduction in crystallinity could aggravate the particle microcracking, which lowers the electrical contact between the current collector and cathode, leading to capacity loss [62].

As such, the discharge capacity in L1.00 increases from 94.9 mAh/g (1st cycle) to the largest capacity of 254.5 mAh/g (46th cycle) and stabilize at 252 mAh/g at 0.1C, maintaining a reversible
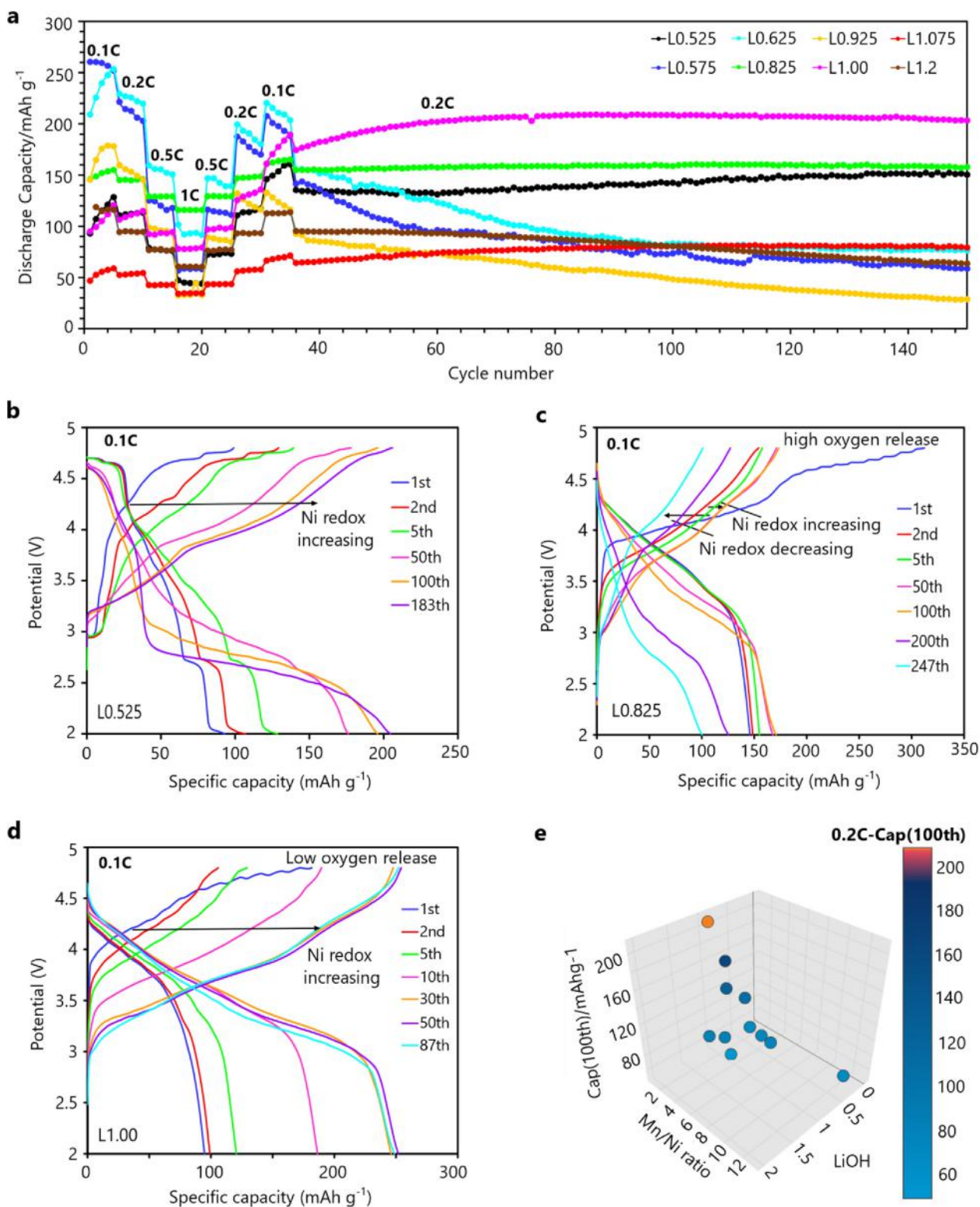
Fig. 4. (a) rate capability of the products when cycling between 2.0 and 4.8 V at various rates from 0.1 to 1 C at room temperature; (b) selected charge−discharge profiles of the L0.525, (c) L0.825, and (d) L1.00 cathode; (e) Full experimental history of random seeds with highlighted best sample from the viewpoint of capacity.

capacity retention ratio above 99% of its maximum discharge capacity even after 85 cycles (Fig. 4d). When cycled at 0.2 C, L1.00 shows the maximum discharge capacity of 209.2 (87th cycle) with 97% capacity retention after 150 cycles (see Fig. 4a and Supplementary Note3 for details). As shown in first charge curve of L1.00

(Fig. 4d), the oxidation peak around 4.8 V related to the activation process has a lower intensity due to formation of oxygen vacancy comparison with other layered LMNO products (L0.825 and L0.925), although the Ni and oxygen redox has a higher intensity in the following cycles. The reversible Ni and anionic redox lead to an

improvement of the capacity of L1.00 sample and is discussed in detail in later.

Increasing Li content in L1.075 results in the first charge and discharge capacity of 135 and 47 mAh/g, which increases afterward upon cycling prior to stabilize at 147.0 mAh/g after 32 cycles at 0.1C (Fig. S13) and 82 mAh/g after 108 cycles at 0.2C (Fig. 2a) due to surface Mn/Ni~2. Moreover, L1.2 has first charge and discharge capacity of 252.9 and 102.5 mAh/g at 0.1C, which discharge capacity decays to 64 mAh/g after 150 cycles at 0.2C.

The charge profiles of L1.075 and L1.2 show that the amount of LiTMO$_2$ composition is much less than Li$_2$MnO$_3$ phase due to the formation of higher Li-rich phase caused by introducing high Li ions into materials. Consequently, Ni redox reduces as a decrease in the slant curve from 3 to 4.5 V in L1.075 and L1.2 electrodes compared with L1.00 (Fig. S13), thereby severe capacity reduction can be observed. As shown in Fig. 4d, the first cationic redox (from 3 to 4.5 V in first charge profile) exhibits specific capacities of ~70 mAh/g, which increases during cycling. Moreover, the specific capacities above 4.5 V in first charge is related to anionic redox. In subsequent cycles, the cationic and anionic redox are increasing to ~250 mAh/g due to surface Mn/Ni~2 and high amount of surface oxygen vacancies. The growing of Ni and oxygen redox during cycling has been further confirmed by CV analysis of L1.00 sample over extensive cycling, which is presented in Fig. 5b.

However, the first cationic redox for L1.075 sample shows specific capacities of ~20 mAh/g, which is much less than L1.00 (as shown in Fig. S13). Although, the cationic redox in L1.075 grows during cycling, however, the maximum charge capacities after 100 cycles reaches to 110 mAh/g. Likewise, for L1.2 sample, the cationic redox in first cycle exhibits ~80 mAh/g without stepwise capacity increasing over cycling. Therefore, the maximum cationic redox of L1.2 is lower than L1.00, which is shown in Fig. S13.

Furthermore, the larger irreversible Li$_2$MnO$_3$ activation process can be observed for the L1.075 and L1.2 samples compared to L1.00 due to high Li content along with lower surface oxygen vacancies, which lead to loss of electrochemically active lithium sites and oxygen. From Fig. S13 correspond to L1.2 sample and Fig. 5a, it can be found that there is a large Li$_2$MnO$_3$ phase activation plateau even during the second cycle leading to higher irreversible oxygen redox. The charge capacity after 1st, 2nd and 3rd cycles are 253, 175, and 123 mAh/g, respectively, which demonstrates the large irreversible capacity loss.

3.3.1. Study the appropriate Mn/Ni ratio for CG-LMNO structures

Interestingly, the optimum materials for long-term cycling stability were L0.525, L0.825, and L1.00, which have a lower Mn/Ni ratio (≤ 2) and obtained by stabilizing the cationic redox chemistry (Fig. 4e). Based on the galvanostatic results, the occurred redox
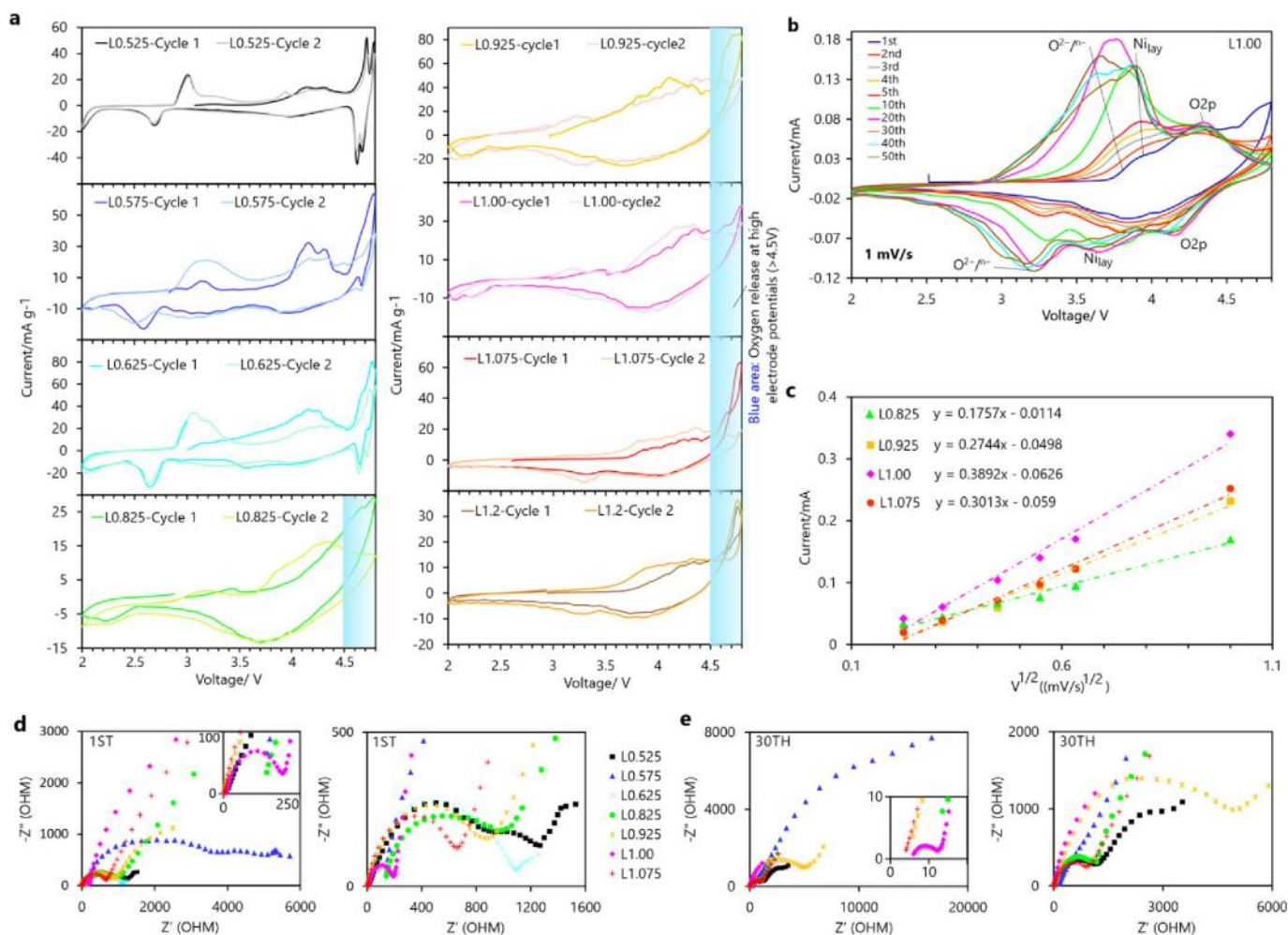

Fig. 5. Oxygen vacancy evaluation on the electrochemical properties of LMNO cathodes. The initial CV curves of (a) L0.525-L1.2 samples at 0.05 mV/s, (b) CV plots for L1.00 at 1 mV/s, (c) Linear relationship of the peak current (I$_p$) and the square root of the scanning rate (v$^{1/2}$), I$_p$ = kD$_{Li^+}^{1/2}$ $\vartheta^{1/2}$ (k is constant) for L0.825-L1.075 electrodes, (d) EIS results of materials after 1st and (e) after 30th cycle.

reactions around 4 V are attributed to Ni^{2+}, which are gradually developed over cycles. This prevents the extraction of more Li^+ from the lattice, which causes the cation migration. Thus, Li^+ ions are gradually involved in the reactions, increasing the capacity during cycling and overall stability. In addition, L1.00 has better rate property than L0.525 sample with similar stepwise capacity increase and initial charge capacity, with a maximum charge capacity of about 116.7 mAh/g at 0.2C, 94.9 mAh/g at 0.5C, and 78.5 mAh/g at 1C-rate, respectively.

Among the cathodes with stepwise capacity increase behavior, the L1.00 cathode shows higher extent of reversible Ni^{2+} redox, this is because of two reasons; high Ni content and cation mixing. To investigate the structural properties of the materials and origins of the above results, thermodynamic stability of the $LiMnO_2$, $LiNi_{0.2}Mn_{0.8}O_2$, $LiNi_{0.3}Mn_{0.7}O_2$, and $LiNi_{0.5}Mn_{0.5}O_2$, we calculated their formation energy using DFT calculations. As shown in Fig. S18, the formation energy of structures is clearly decreased by increasing Ni ratio, resulting in more stable structures which confirms the structural stability of L1.00 sample.

This result in agreement with previous studies that indicated increasing the Ni content in LLO materials has been lead to lessen the structure degradation and improve cyclic stability and rate performance by inhibiting the layered-to-spinel phase transformation [37,63,64]. Ni ions can migrate out from the Li layer because of the larger ionic radius of Ni ions relative to Mn ions, which tend to be trapped in dumbbells; thus, prevents continuous migration of TM ions to Li sites by reversible migrating between TM layer and interlayer, inhibiting Li—Li dumbbell and layered-spinel transition as a pillar.

Likewise, as summarized in Table 1, L1.00 shows higher cation mixing and disordered structure, which may arise from the high Ni content and oxygen vacancies. Some scholars believe that the cation mixing of L1.00 plays a positive role in retarding structural rearrangement through supporting the Li slabs and reducing repulsion of neighboring oxygen layers during the gradual delithiation process and Ni^{2+}/Ni^{4+} redox [26], which good agreement with our result. Therefore, the appropriate amount of surface Mn/Ni ratio, high Ni content and calcination temperature will be needed to optimize structural crystallinity and cation mixing of LLO cathodes.

3.3.2. Evaluate the redox properties of TM ions

The corresponding CV experiments of cathodes have been carried out to evaluate the redox potential of the TM ions (Fig. 5a). L0.525-L0.625 manifest typical spinel redox features, in which the anodic peaks at ~3—3.2 V/3.8, ~4.1, and ~4.7/4.8 V are attributed to Mn^{3+}/Mn^{4+}, and Ni^{2+}/Ni^{4+} redox in spinel phase, respectively [65]. Moreover, the CV curves of L0.525-L0.625 confirm the formation of the second layered LLO phase, indicating that the anodic peaks at ~4.15/4.3 V and ~4.6—4.8 V are ascribed to the Ni^{2+}/Ni^{4+} and Li_2MnO_3 activation, respectively. Taken together, the charge compensation of Li removal at ~4.6—4.8 V would result in reversible as well as irreversible anionic redox accompanied by significant oxygen loss from the surface. A reduction process corresponding to the activation process involves two reversible contributions, (1) O_{2p} and (2) $O^{2-}/^{n-}$ [66,67]. O_{2p} is attributed to the formation of electron holes in the O_{2p} band coordinated by Mn^{4+} and Li^+ ions during the Li^+ removal [9]; while $O^{2-}/^{n-}$ is ascribed to a reversible $O^{2-}/^{n-}$ contribution [66,67]. Likewise, in the CV profiles of L0.825-L1.2, the peaks of LLO are observed. Details of the CV results can be found in the supplementary Note4.

The CV curves for some of samples were not closed due to passivation of the electrodes and improvement of Li ions and electron transfer kinetic. In composites with spinel phase, the voltage at the beginning of charging is associated with the nickel redox voltage. But with increasing cycle, the nickel redox increases

due to the improvement of ion kinetics and electron transfer. Thus, the current at the beginning and end of the cycle is different, leading to creation of non-closed CV curve. Also, another point is related to passivation, which can be seen especially in layered phases. It occurs when the passivating compound is deposited on the electrodes and causes the reduction of reaction rate. Therefore, the peak potential shifts to more negative and positive in cathodic and anodic reactions, respectively.

3.3.3. The role of oxygen vacancies on the L1.00 electrochemical properties

Previous studies have been reported that during the activation of Li_2MnO_3 phase, the active lattice oxygen (O_O) in LLO transformed to some surface oxygen vacancies (V_O) and oxygen gas (O_2), assuming oxygen release in the form of gas. Thus, this reaction can be simplified as follows [12]: $O_O \rightarrow \frac{1}{2}O_2 + V_{\ddot{O}} + 2e^-$. By considering the chemical activity of O_O is equal to 1 and the concentration of generated e^- is twice that of V_O ($[e^-] = 2[V_{\ddot{O}}]$), the equilibrium constant of this reaction can be written as $K = 4[V_{\ddot{O}}]^3 P_{O_2}^{1/2}$, and consequently, $P_{O_2} = K'[V_{\ddot{O}}]^{-6}$ in which $K' = \frac{K}{4}$.

Based on the equations, the oxygen partial pressure (P_{O_2}) depends on the content of the oxygen vacancies ($V_{\ddot{O}}$), and the creation of surface oxygen vacancies is accompanied by a less oxygen release [12].

Thus, evidence of surface oxygen vacancies on the electrochemical performance of our samples is observed in.

(1) Inhibiting oxygen release above 4.5 V. Hence, the initial two CV curves of the samples were studied to evaluate the oxygen release from cathodes with different oxygen vacancies. For this aim, the samples with single LLO phase were compared to eliminate the effect of spinel redox peaks (can be seen in Fig. 5a). The blue regions in CV curves correspond to oxygen evolution from the cathodes. As mentioned before, the contributions of oxygen redox are O_{2p} (>4.5 V) and $O^{2-}/^{n-}$ (~3.3 V) redoxes. The difference between the first and second oxygen oxidation peak above 4.5 V (O_{2p}) in L1.00 is smaller than the other samples due to the existence of more oxygen vacancies on its surface, inhibiting the irreversible oxygen release.

For emphasizing the occurring redox processes, the CV profiles of L1.00 sample during extensive cycling are presented in Fig. 5b. The CV result reveals that the O_{2P} peak does not possess capacity fading, indicating that the released oxygen for the L1.00 cathode is very low. Furthermore, during the initial charge-discharge of the L1.00 material, the broad peak around 4.3 V is attributed to $O^{2-}/^{n-}$ as well as Ni^{2+}/Ni^{4+} redox, while $O^{2-}/^{n-}$ and Ni^{2+}/Ni^{4+} extensively developed in oxidation and reduction peaks in addition to the slight increase of O_{2p}, which confirms the stepwise capacity increasing of L1.00 sample.

(2) reduction decomposition of electrolyte and improving of conductivity at the cathode/electrolyte interface due to suppression of the reactive oxygen radicals from formation on the cathode' surface upon de/lithiation process.

To evaluate this item, the conductivity is further investigated utilizing the EIS analysis from cathode materials. EIS measurements were performed for pristine samples and after equilibrium at a charged state of 4.8 V from 1st, 10th, 20th and 30th cycles (Fig. S20). An entire Li-ion battery cell can be modeled using an equivalent circuit shown in Fig. S21, in which the R_b, R_{SEI}, R_{ct}, and W

Table 3
Comparison with recent reported Co-free LLO cathodes.

Cathode materials	Test conditions (mA/g)	Charge/discharge capacity (mAh/g)	Capacity Retention	Method	Refs.
$Li(Li_{0.17}Mn_{0.55}Ni_{0.28})O_2$	20	254	99% (after 85 cycles)	Polyol-assisted	This work
$Li(Li_{0.2}Mn_{0.6}Ni_{0.2})O_2$	48	220	93% (after 100 cycles)	Co-precipitation	[30]
$Li(Li_{0.2}Mn_{0.6}Ni_{0.2})O_2$	32	240	88% (after 50 cycles)	Co-precipitation	[46]
$Li(Li_{0.2}Mn_{0.6}Ni_{0.2})O_2$	35	220	85% (after 100 cycles)	Co-precipitation	[70]
$Li(Li_{0.2}Mn_{0.6}Ni_{0.2})O_2$	250	205	84% (after 100 cycles)	Sol-gel	[71]
$Li(Li_{0.2}Mn_{0.6}Ni_{0.2})O_2$	5	220	76% (after 40 cycles)	Sol-gel	[13]
$Li(Li_{0.2}Mn_{0.6}Ni_{0.2})O_2$	100	187	75% (after 100 cycles)	Combustion	[72]
$Li(Li_{0.2}Mn_{0.53}Ni_{0.27})O_2$	250	199	50% (after 200 cycles)	Co-precipitation	[73]
$Li(Li_{0.17}Mn_{0.58}Ni_{0.25})O_2$	20	226	22% (after 80 cycles)	Co-precipitation	[74]

As a result, this advantage of the L1.00 cathode could be attributed to increasing oxygen vacancies at high calcination temperature under reducing atmosphere as well as high Ni/Mn ratio on its surface and Li/Ni cation mixing.

parameters stand for the internal resistance of the cell, solid-electrolyte interface resistance, charge transfer resistance, and Warburg element, respectively [68].

The first semicircle of the EIS spectrum originates from the impedance of a layer that forms on the interface between the electrode and electrolyte. This interfacial layer is called the solid electrolyte interphase (SEI) layer, and it is generated by the decomposition of the electrolyte. It was found that R_{SEI} is extremely sensitive to the reactivity of the electrolyte during the first lithiation cycle, which released oxygen and Mn dissolution could affect its reactivity. As clearly observed in Fig. 5d and e, the R_{SEI} results of the electrodes after the 1st cycle are in order: L0.575 > L0.625 ~ L0.525 > L0.825 > L0.925 > L1.075 > L1.00. L1.00 cathode has the smaller R_{SEI} after the first charging due to low released oxygen and high Ni content on the surface, thereby reducing electrolyte decomposition. Whereas the L0.625 and L0.575 have higher R_{SEI} due to more Mn on their surface, consequently Mn dissolution into the electrolyte because of its reaction with released oxygen. L1.00 keeps this trend after the 30th cycle: L0.575 > L0.825 > L0.925 > L0.825 > L0.525 > L1.075 > L1.00.

And (3) increasing of Li^+ diffusion and ionic conductivity. Oxygen vacancies in the LLO electrochemical properties is increasing of Li^+ diffusion and ionic conductivity. From the research on the Li^+ migration from the octahedral sites in Li layer to TM layer through intermediary tetrahedral sites, there is a high chance of escaping the trapped Li^+ in the tetrahedral sites (Li–Li dumbbells) with introduction the oxygen vacancy. So, the favorable Li^+ diffusion into adjacent octahedral sites leads to increased ionic conductivity [12].

For calculating the Li^+ diffusion for products, the CV curves were studied at different scanning rates, which are shown in Fig. S22. Fitting the linear relationship between the peak currents and the square root of the scanning rate for peaks yields comparable Li ion apparent diffusion coefficient D_{Li} values to those for the cathode materials, according to the Randles Sevick equation:

$$I_p = \left(2.69 \times 10^5\right) n^{3/2} A D_{Li+}^{1/2} C_{Li+} \vartheta^{1/2} \tag{8}$$

where Ip is the peak current of anodic or cathodic peaks, n is the number of electrons per formula during the insertion, A is the effective contact area between the electrode and electrolyte, C_{Li+} is the concentration of Li^+ in the cathode, D_{Li} is the diffusion coefficient of Li, and ϑ is the scan rate [69].

Based on Eq. (8), the fitted slopes of the different electrodes are calculated and shown in Fig. 5c. Apparently, the D_{Li+} at the voltage of O_{2P} reaction for L1.00, which is proportional to its slope, is higher than other electrodes due to lower irreversible oxygen loss in the initial charge. Of course, the mesoscopic structure could enhance the Li^+ diffusion due to more surface area. Thus, both the creation of oxygen vacancies and mesostructure design play a positive role in Li^+ diffusion.

Further, the second semicircle in the EIS results is related to the R_{ct}, which is linked to the kinetics of an electrochemical reactions that occur during the charge-discharge process [68]. Hence, by comparing the R_{ct}(1st) results: L1.2 > L1.075 > L1.00 > L0.825 > L0.925 > L0.525 > L0.625 > L0.575, the higher electronic conductivity of L0.525, L0.575, and L0.625 should be essentially attributed to the spinel phase with 3D Li-ion diffusion channels, which leads to higher capacity especially in initial cycles, as previously discussed. As such, in layered structures, the cathodes with lower Li content possess better charge transfer due to higher Li^+ concentration-gradient during intercalation process, which facilitates the surface kinetics of L1.00, and L0.825 electrodes upon cycling.

At the same time, the R_{ct} after 30th could be observed in the following order: L0.575 > L1.075 > L0.825 > L1.00 > L0.525. Thus, the L0.525, L1.00, L0.825, and L1.075 samples have the smallest R_{ct}(30th), respectively, which is coinciding with the galvanostatic results. Thus, a stepwise capacity increase of electrodes over long term cycling could be ascribed to lower R_{ct} and high Ni/Mn ratio on LLO's surface.

According to the results, we could prioritize the factors influencing the R_{ct}: Firstly, the high Ni/Mn ratio on LLO's surface, and presence of the spinel phase, which can be seen in comparison of L0.525 with other LLO-CG structures; secondly, surface oxygen vacancies, and mesoscopic structure by comparison of L1.00 with L0.825. The creation of oxygen vacancy has a considerable effect in reducing charge-transfer resistance for Li^+ migration and less electrode polarization, demonstrating a lower chance of trapping the Li-ion in the Li–Li dumbbells, thereby ionic conductivity improvement [12] (see Supplementary Note5 for details). Thus, the R_{ct} and R_{SEI} of L1.00 after 30th cycle reveals that oxygen vacancy introduction in CG-LLO with surface Mn/Ni~1.5 accompanied by mesoscopic structure has a considerable effect in reducing interfacial and charge-transfer resistance.

To summarize, we herein employed random seeds to explore the various synthesis parameters more efficiently and find the optimal synthesis conditions to design the LMNO cathodes that satisfy the electrochemical properties such as large capacity, long cycle life, and good rate capability (Fig. S23). Based on our investigation, L1.00 was found to give the best performance with namely the large capacity, cycle life and rate capability (Fig. 4c), see Supplementary Note6 for details. Our best capacity and those of others are provided in Table 3, suggesting that the prepared Co-free LLO can be used as a promising cathode material for Li-ion battery.

4. Conclusion

In summary, this work provides practical approaches that will help resolve irreversible anionic and cationic redox issues by engineering the cathode/electrolyte interface and structure. We

proposed a new strategy to improve the electrochemical performances of Co-free LLO synthesized via a polyol-assisted method by integrating oxygen vacancies and the high Ni/Mn ratio on LLO's surface (Mn/Ni~1.5). The specific amount of oxygen vacancies on the surface of as-synthesized LLO cathodes plays a crucial role in improving electrochemical performance due to less oxygen generation during cycling and driving the reversible anionic redox processes, decreasing the interfacial and charge transfer resistance of Li^+ diffusion. At the same time, high Ni segregation on the surface of concentration-gradient layered and spinel/layered Li-rich materials with the ratio of Mn/Ni $\leq$ 2 leads to a higher lithium diffusion barrier near the surface region. Consequently, stepwise capacity increase is associated with enhanced specific capacity and better cycling capability. Therefore, we conclude that the high capacity in L1.00 is mainly attributed to reversible anionic redox processes and cationic redox of Ni^{2+}/Ni^{4+}. This study offers the simple, versatile, low-cost, and scalable approach to control the oxygen vacancy, and surface Mn/Ni content in Co-free concentration-gradient Li-rich oxides, highlighting their promise as high-capacity cathodes.

CRediT author statement

Parisa Vahdatkhah: Conceptualization, Investigation, Methodology, Data Curation, Writing- Original draft preparation, Writing − review & editing.

Oleksandr Voznyy: Supervision, Formal analysis, Software, Resources, Funding acquisition, Writing − review & editing.

S.K. Sadrnezhaad: Supervision, Formal analysis, Resources, Funding acquisition, Writing- Reviewing and Editing.

Declaration of competing interest

Data availability

Data will be made available on request.

Acknowledgment

Appendix A. Supplementary data

Supplementary data to this article can be found online at https://doi.org/10.1016/j.mtsust.2022.100309.

References

[1] M. Sathiya, G. Rousse, K. Ramesha, C.P. Laisa, H. Vezin, M.T. Sougrati, M.-L. Doublet, D. Foix, D. Gonbeau, W. Walker, A.S. Prakash, M. Ben Hassine, L. Dupont, J.-M. Tarascon, Reversible anionic redox chemistry in high-capacity layered-oxide electrodes, Nat. Mater. 12 (9) (2013) 827−835, https://doi.org/10.1038/nmat3699.

[2] D. Ye, G. Zeng, K. Nogita, K. Ozawa, M. Hankel, D.J. Searles, L. Wang, Understanding the origin of Li2MnO3 activation in Li-rich cathode materials for lithium-ion batteries, Adv. Funct. Mater. 25 (48) (2015) 7488−7496, https://doi.org/10.1002/adfm.201503276.

[3] T. Lin, T.U. Schulli, Y. Hu, X. Zhu, Q. Gu, B. Luo, B. Cowie, L. Wang, Faster activation and slower capacity/voltage fading: a bifunctional urea treatment on lithium-rich cathode materials, Adv. Funct. Mater. 30 (13) (2020), 1909192, https://doi.org/10.1002/adfm.201909192.

[4] H. Koga, L. Croguennec, M. Ménétrier, P. Mannessiez, F. Weill, C. Delmas, Different oxygen redox participation for bulk and surface: a possible global explanation for the cycling mechanism of Li1.20Mn0.54Co0.13Ni0.13O2, J. Power Sources 236 (2013) 250−258, https://doi.org/10.1016/j.jpowsour.2013.02.075.

[5] W.E. Gent, K. Lim, Y. Liang, Q. Li, T. Barnes, S.-J. Ahn, K.H. Stone, M. McIntire, J. Hong, J.H. Song, Y. Li, A. Mehta, S. Ermon, T. Tyliszczak, D. Kilcoyne, D. Vine, J.-H. Park, S.-K. Doo, M.F. Toney, W. Yang, D. Prendergast, W.C. Chueh, Coupling between oxygen redox and cation migration explains unusual electrochemistry in lithium-rich layered oxides, Nat. Commun. 8 (1) (2017) 2091, https://doi.org/10.1038/s41467-017-02041-x.

[6] X. Ji, Q. Xia, Y. Xu, H. Feng, P. Wang, Q. Tan, A review on progress of lithium-rich manganese-based cathodes for lithium ion batteries, J. Power Sources 487 (2021), 229362, https://doi.org/10.1016/j.jpowsour.2020.229362.

[7] X. Li, Y. Qiao, S. Guo, Z. Xu, H. Zhu, X. Zhang, Y. Yuan, P. He, M. Ishida, H. Zhou, Direct visualization of the reversible O2−/O− redox process in Li-rich cathode materials, Adv. Mater. 30 (14) (2018), 1705197, https://doi.org/10.1002/adma.201705197.

[8] J. Zhang, F. Cheng, S. Chou, J. Wang, L. Gu, H. Wang, H. Yoshikawa, Y. Lu, J. Chen, Tuning oxygen redox chemistry in Li-rich Mn-based layered oxide cathodes by modulating cation arrangement, Adv. Mater. 31 (42) (2019), 1901808, https://doi.org/10.1002/adma.201901808.

[9] K. Luo, M.R. Roberts, R. Hao, N. Guerrini, D.M. Pickup, Y.-S. Liu, K. Edström, J. Guo, A.V. Chadwick, L.C. Duda, P.G. Bruce, Charge-compensation in 3d-transition-metal-oxide intercalation cathodes through the generation of localized electron holes on oxygen, Nat. Chem. 8 (7) (2016) 684−691, https://doi.org/10.1038/nchem.2471.

[10] D.-H. Seo, J. Lee, A. Urban, R. Malik, S. Kang, G. Ceder, The structural and chemical origin of the oxygen redox activity in layered and cation-disordered Li-excess cathode materials, Nat. Chem. 8 (7) (2016) 692−697, https://doi.org/10.1038/nchem.2524.

[11] Y. Xie, Y. Jin, L. Xiang, Li-rich layered oxides: structure, capacity and voltage fading mechanisms and solving strategies, Particuology 61 (2022) 1−10, https://doi.org/10.1016/j.partic.2021.05.011.

[12] B. Qiu, M. Zhang, L. Wu, J. Wang, Y. Xia, D. Qian, H. Liu, S. Hy, Y. Chen, K. An, Y. Zhu, Z. Liu, Y.S. Meng, Gas−solid interfacial modification of oxygen activity in layered oxide cathodes for lithium-ion batteries, Nat. Commun. 7 (1) (2016), 12108, https://doi.org/10.1038/ncomms12108.

[13] D. Eum, B. Kim, S.J. Kim, H. Park, J. Wu, S.-P. Cho, G. Yoon, M.H. Lee, S.-K. Jung, W. Yang, W.M. Seong, K. Ku, O. Tamwattana, S.K. Park, I. Hwang, K. Kang, Voltage decay and redox asymmetry mitigation by reversible cation migration in lithium-rich layered oxide electrodes, Nat. Mater. 19 (4) (2020) 419−427, https://doi.org/10.1038/s41563-019-0572-4.

[14] E. Hu, X. Yu, R. Lin, X. Bi, J. Lu, S. Bak, K.-W. Nam, H.L. Xin, C. Jaye, D.A. Fischer, K. Amine, X.-Q. Yang, Evolution of redox couples in Li- and Mn-rich cathode materials and mitigation of voltage fade by reducing oxygen release, Nat. Energy 3 (8) (2018) 690−698, https://doi.org/10.1038/s41560-018-0207-z.

[15] B. Xiao, X. Sun, Surface and subsurface reactions of lithium transition metal oxide cathode materials: an overview of the fundamental origins and remedying approaches, Adv. Energy Mater. 8 (29) (2018), 1802057, https://doi.org/10.1002/aenm.201802057.

[16] Z. Zhu, D. Yu, Y. Yang, C. Su, Y. Huang, Y. Dong, I. Waluyo, B. Wang, A. Hunt, X. Yao, J. Lee, W. Xue, J. Li, Gradient Li-rich oxide cathode particles immunized against oxygen release by a molten salt treatment, Nat. Energy 4 (12) (2019) 1049−1058, https://doi.org/10.1038/s41560-019-0508-x.

[17] Q. Chen, Y. Pei, H. Chen, Y. Song, L. Zhen, C.-Y. Xu, P. Xiao, G. Henkelman, Highly reversible oxygen redox in layered compounds enabled by surface polyanions, Nat. Commun. 11 (1) (2020) 3411, https://doi.org/10.1038/s41467-020-17126-3.

[18] Y. Pei, Q. Chen, M. Wang, B. Li, P. Wang, G. Henkelman, L. Zhen, G. Cao, C.-Y. Xu, Reviving reversible anion redox in 3d-transition-metal Li rich oxides by introducing surface defects, Nano Energy 71 (2020), 104644, https://doi.org/10.1016/j.nanoen.2020.104644.

[19] R. Sharpe, R.A. House, M.J. Clarke, D. Förstermann, J.-J. Marie, G. Cibin, K.-J. Zhou, H.Y. Playford, P.G. Bruce, M.S. Islam, Redox chemistry and the role of trapped molecular O2 in Li-rich disordered rocksalt oxyfluoride cathodes, J. Am. Chem. Soc. 142 (52) (2020) 21799−21809, https://doi.org/10.1021/jacs.0c10270.

[20] K. Kubota, T. Kaneko, M. Hirayama, M. Yonemura, Y. Imanari, K. Nakane, R. Kanno, Direct synthesis of oxygen-deficient Li2MnO3−x for high capacity lithium battery electrodes, J. Power Sources 216 (2012) 249−255, https://doi.org/10.1016/j.jpowsour.2012.05.061.

[21] J. Zhao, R. Huang, W. Gao, J.-M. Zuo, X.F. Zhang, S.T. Misture, Y. Chen, J.V. Lockard, B. Zhang, S. Guo, M.R. Khoshi, K. Dooley, H. He, Y. Wang, An ion-exchange promoted phase transition in a Li-excess layered cathode material for high-performance lithium ion batteries, Adv. Energy Mater. 5 (9) (2015), 1401937, https://doi.org/10.1002/aenm.201401937.

[22] T. Nakamura, K. Ohta, Y. Kimura, K. Tsuruta, Y. Tamenori, R. Aso, H. Yoshida, K. Amezawa, Impact of oxygen defects on electrochemical processes and charge compensation of Li-rich cathode material Li1.2Mn0.6Ni0.2O2−δ, ACS Appl. Energy Mater. 3 (10) (2020) 9703−9713, https://doi.org/10.1021/acsaem.0c01303.

[23] S.-H. Kang, C.S. Johnson, J.T. Vaughey, K. Amine, M.M. Thackeray, The effects of acid treatment on the electrochemical properties of 0.5 Li[sub 2]MnO[sub 3]· 0.5 LiNi[sub 0.44]Co[sub 0.25]Mn[sub 0.31]O[sub 2] electrodes in lithium cells, J. Electrochem. Soc. 153 (6) (2006) A1186, https://doi.org/10.1149/1.2194764.

[24] B. Song, H. Liu, Z. Liu, P. Xiao, M.O. Lai, L. Lu, High rate capability caused by surface cubic spinels in Li-rich layer-structured cathodes for Li-ion batteries, Sci. Rep. 3 (1) (2013) 3094, https://doi.org/10.1038/srep03094.

[25] Q. Li, D. Ning, D. Zhou, K. An, D. Wong, L. Zhang, Z. Chen, G. Schuck, C. Schulz, Z. Xu, G. Schumacher, X. Liu, The effect of oxygen vacancy and spinel phase integration on both anionic and cationic redox in Li-rich cathode materials, J. Mater. Chem. A 8 (16) (2020) 7733−7745, https://doi.org/10.1039/D0TA02517H.

[26] J.-L. Shi, J.-N. Zhang, M. He, X.-D. Zhang, Y.-X. Yin, H. Li, Y.-G. Guo, L. Gu, L.-J. Wan, Mitigating voltage decay of Li-rich cathode material via increasing Ni content for lithium-ion batteries, ACS Appl. Mater. Interfaces 8 (31) (2016) 20138−20146, https://doi.org/10.1021/acsami.6b06733.

[27] R.C. Longo, C. Liang, F. Kong, K. Cho, Core−shell nanocomposites for improving the structural stability of Li-rich layered oxide cathode materials for Li-ion batteries, ACS Appl. Mater. Interfaces 10 (22) (2018) 19226−19234, https://doi.org/10.1021/acsami.8b03898.

[28] M. Zhang, H. Liu, Z. Liu, C. Fang, Y.S. Meng, Modified coprecipitation synthesis of mesostructure-controlled Li-rich layered oxides for minimizing voltage degradation, ACS Appl. Energy Mater. 1 (7) (2018) 3369−3376, https://doi.org/10.1021/acsaem.8b00545.

[29] R. Yu, X. Zhang, T. Liu, L. Yang, L. Liu, Y. Wang, X. Wang, H. Shu, X. Yang, Spinel/layered heterostructured lithium-rich oxide nanowires as cathode material for high-energy lithium-ion batteries, ACS Appl. Mater. Interfaces 9 (47) (2017) 41210−41223, https://doi.org/10.1021/acsami.7b11942.

[30] Y. Liu, X. Fan, Z. Zhang, H.-H. Wu, D. Liu, A. Dou, M. Su, Q. Zhang, D. Chu, Enhanced electrochemical performance of Li-rich layered cathode materials by combined Cr doping and LiAlO2 coating, ACS Sustain. Chem. Eng. 7 (2) (2019) 2225−2235, https://doi.org/10.1021/acssuschemeng.8b04905.

[31] H. Peng, S.-X. Zhao, C. Huang, L.-Q. Yu, Z.-Q. Fang, G.-D. Wei, In situ construction of spinel coating on the surface of a lithium-rich manganese-based single crystal for inhibiting voltage fade, ACS Appl. Mater. Interfaces 12 (10) (2020) 11579−11588, https://doi.org/10.1021/acsami.9b21271.

[32] Y. Liu, Z. Yang, J. Zhong, J. Li, R. Li, Y. Yu, F. Kang, Surface-functionalized coating for lithium-rich cathode material to achieve ultra-high rate and excellent cycle performance, ACS Nano 13 (10) (2019) 11891−11900, https://doi.org/10.1021/acsnano.9b05960.

[33] F. Ding, J. Li, F. Deng, G. Xu, Y. Liu, K. Yang, F. Kang, Surface heterostructure induced by PrPO4 modification in Li1.2[Mn0.54Ni0.13Co0.13]O2 cathode material for high-performance lithium batteries with mitigating voltage decay, ACS Appl. Mater. Interfaces 9 (33) (2017) 27936−27945, https://doi.org/10.1021/acsami.7b07221.

[34] P. Vahdatkhah, S. Khatiboleslam Sadrnezhaad, O. Voznyy, On the functionality of the polypyrrole nanostructures for surface modification of Co-free Li-rich layered oxide cathode applied in lithium-ion batteries, J. Electroanal. Chem. 914 (2022), 116317, https://doi.org/10.1016/j.jelechem.2022.116317.

[35] Y. Yu, Z. Yang, J. Zhong, Y. Liu, J. Li, X. Wang, F. Kang, A simple dual-ion doping method for stabilizing Li-rich materials and suppressing voltage decay, ACS Appl. Mater. Interfaces 12 (12) (2020) 13996−14004, https://doi.org/10.1021/acsami.0c00944.

[36] Z. Yu, F. Ning, B. Li, Z. Sun, W. Chu, D. Xia, Mitigating voltage decay of Li-rich layered oxide by incorporation of 5d metal rhenium, J. Phys. Chem. C 123 (31) (2019) 18870−18876, https://doi.org/10.1021/acs.jpcc.9b05683.

[37] S. Chen, Z. Chen, M. Xia, C. Cao, Y. Luo, Toward alleviating voltage decay by sodium substitution in lithium-rich manganese-based oxide cathodes, ACS Appl. Energy Mater. 1 (8) (2018) 4065−4074, https://doi.org/10.1021/acsaem.8b00740.

[38] W. Liu, J. Li, W. Li, H. Xu, C. Zhang, X. Qiu, Inhibition of transition metals dissolution in cobalt-free cathode with ultrathin robust interphase in concentrated electrolyte, Nat. Commun. 11 (1) (2020) 3629, https://doi.org/10.1038/s41467-020-17396-x.

[39] C. Cui, X. Fan, X. Zhou, J. Chen, Q. Wang, L. Ma, C. Yang, E. Hu, X.-Q. Yang, C. Wang, Structure and interface design enable stable Li-rich cathode, J. Am. Chem. Soc. 142 (19) (2020) 8918−8927, https://doi.org/10.1021/jacs.0c02302.

[40] T. Wu, X. Liu, X. Zhang, Y. Lu, B. Wang, Q. Deng, Y. Yang, E. Wang, Z. Lyu, Y. Li, Y. Wang, Y. Lyu, C. He, Y. Ren, G. Xu, X. Sun, K. Amine, H. Yu, Full concentration gradient-tailored Li-rich layered oxides for high-energy lithium-ion batteries, Adv. Mater. 33 (2) (2021), 2001358, https://doi.org/10.1002/adma.202001358.

[41] X. Ju, X. Hou, Z. Liu, H. Zheng, H. Huang, B. Qu, T. Wang, Q. Li, J. Li, The Full gradient design in Li-rich cathode for high performance lithium ion batteries with reduced voltage decay, J. Power Sources 437 (2019), 226902, https://doi.org/10.1016/j.jpowsour.2019.226902.

[42] P. Hou, G. Li, X. Gao, Tailoring atomic distribution in micron-sized and spherical Li-rich layered oxides as cathode materials for advanced lithium-ion batteries, J. Mater. Chem. A 4 (20) (2016) 7689−7699, https://doi.org/10.1039/C6TA01878E.

[43] A. Celeste, M. Tuccillo, A. Santoni, P. Reale, S. Brutti, L. Silvestri, Exploring a Co-free, Li-rich layered oxide with low content of nickel as a positive electrode for Li-ion battery, ACS Appl. Energy Mater. 4 (10) (2021) 11290−11297, https://doi.org/10.1021/acsaem.1c02133.

[44] H. Chung, A. Grenier, R. Huang, X. Wang, Z. Lebens-Higgins, J.-M. Doux, S. Sallis, C. Song, P. Ercius, K. Chapman, L.F.J. Piper, H.-M. Cho, M. Zhang, Y.S. Meng, Comprehensive study of a versatile polyol synthesis approach for cathode materials for Li-ion batteries, Nano Res. 12 (9) (2019) 2238−2249, https://doi.org/10.1007/s12274-019-2494-5.

[45] P. Vahdatkhah, H.R. Madaah Hosseini, A. Khodaei, A.R. Montazerabadi, R. Irajirad, M.A. Oghabian, H.,H. Delavari, Rapid microwave-assisted synthesis of PVP-coated ultrasmall gadolinium oxide nanoparticles for magnetic resonance imaging, Chem. Phys. 453−454 (2015) 35−41, https://doi.org/10.1016/j.chemphys.2015.03.007.

[46] W. Hua, S. Wang, M. Knapp, S.J. Leake, A. Senyshyn, C. Richter, M. Yavuz, J.R. Binder, C.P. Grey, H. Ehrenberg, S. Indris, B. Schwarz, Structural insights into the formation and voltage degradation of lithium- and manganese-rich layered oxides, Nat. Commun. 10 (1) (2019) 5365, https://doi.org/10.1038/s41467-019-13240-z.

[47] F. Fievet, F. Fievet-Vincent, J.-P. Lagier, B. Dumont, M. Figlarz, Controlled nucleation and growth of micrometre-size copper particles prepared by the polyol process, J. Mater. Chem. 3 (6) (1993) 627−632, https://doi.org/10.1039/JM9930300627.

[48] L. Wu, L. Yao, B. Hu, S.-H. Yu, Unique lamellar sodium/potassium iron oxide nanosheets: facile microwave-assisted synthesis and magnetic and electrochemical properties, Chem. Mater. 23 (17) (2011) 3946−3952, https://doi.org/10.1021/cm2013736.

[49] S. Lee, S. Wang, C. Wern, S. Yi, The green synthesis of 2D copper nanosheets and their light absorption, Materials (2021), https://doi.org/10.3390/ma14081926.

[50] Y. Shi, M. Zhang, C. Fang, Y.S. Meng, Urea-based hydrothermal synthesis of LiNi0.5Co0.2Mn0.3O2 cathode material for Li-ion battery, J. Power Sources 394 (2018) 114−121, https://doi.org/10.1016/j.jpowsour.2018.05.030.

[51] Y. Pei, C.-Y. Xu, Y.-C. Xiao, Q. Chen, B. Huang, B. Li, S. Li, L. Zhen, G. Cao, Phase transition induced synthesis of layered/spinel heterostructure with enhanced electrochemical properties, Adv. Funct. Mater. 27 (7) (2017), 1604349, https://doi.org/10.1002/adfm.201604349.

[52] M. Jiang, Q. Zhang, X. Wu, Z. Chen, D.L. Danilov, R.-A. Eichel, P.H.L. Notten, Synthesis of Ni-rich layered-oxide nanomaterials with enhanced Li-ion diffusion pathways as high-rate cathodes for Li-ion batteries, ACS Appl. Energy Mater. 3 (7) (2020) 6583−6590, https://doi.org/10.1021/acsaem.0c00765.

[53] H. Zeynali, S. Behnam Mousavi, S.M. Hosseinpour-Mashkani, Synthesis and characterization of Bi/Bi2S3 nanocomposite through polyol method and its photovoltaic applications, Mater. Lett. 144 (2015) 65−68, https://doi.org/10.1016/j.matlet.2015.01.023.

[54] G.-Z. Wei, X. Lu, F.-S. Ke, L. Huang, J.-T. Li, Z.-X. Wang, Z.-Y. Zhou, S.-G. Sun, Crystal habit-tuned nanoplate material of Li[Li1/3−2x/3NixMn2/3−x/3]O2 for high-rate performance lithium-ion batteries, Adv. Mater. 22 (39) (2010) 4364−4367, https://doi.org/10.1002/adma.201001578.

[55] V. Pimenta, M. Sathiya, D. Batuk, A.M. Abakumov, D. Giaume, S. Cassaignon, D. Larcher, J.-M. Tarascon, Synthesis of Li-rich NMC: a comprehensive study, Chem. Mater. 29 (23) (2017) 9923−9936, https://doi.org/10.1021/acs.chemmater.7b03230.

[56] H. Pan, S. Zhang, J. Chen, M. Gao, Y. Liu, T. Zhu, Y. Jiang, Li- and Mn-rich layered oxide cathode materials for lithium-ion batteries: a review from fundamentals to research progress and applications, Mol. Syst. Des. Eng. 3 (5) (2018) 748−803, https://doi.org/10.1039/C8ME00025E.

[57] C. Zhao, X. Wang, X. Liu, H. Zhang, Q. Shen, Mn−Ni content-dependent structures and electrochemical behaviors of serial Li1.2Ni0.13+x-Co0.13Mn0.54−XO2 as lithium-ion battery cathodes, ACS Appl. Mater. Interfaces 6 (4) (2014) 2386−2392, https://doi.org/10.1021/am404690z.

[58] S.-H. Lee, S. Lee, B.-S. Jin, H.-S. Kim, Optimized electrochemical performance of Ni rich LiNi0.91Co0.06Mn0.03O2 cathodes for high-energy lithium ion batteries, Sci. Rep. 9 (1) (2019) 8901, https://doi.org/10.1038/s41598-019-45531-2.

[59] L. Xu, P. Hou, Y. Zhang, H. Zhang, D. Song, X. Shi, X. Wang, L. Zhang, Carbonate coprecipitation preparation of Li-rich layered oxides using the oxalate anion ligand as high-energy, high-power and durable cathode materials for lithium-ion batteries, J. Mater. Chem. A 3 (42) (2015) 21219−21226, https://doi.org/10.1039/C5TA04157K.

[60] X. Ding, D. Luo, J. Cui, H. Xie, Q. Ren, Z. Lin, An ultra-long-life lithium-rich Li1.2Mn0.6Ni0.2O2 cathode by three-in-one surface modification for lithium-ion batteries, Angew. Chem., Int. Ed. 59 (20) (2020) 7778−7782, https://doi.org/10.1002/anie.202000628.

[61] M. Gu, I. Belharouak, A. Genc, Z. Wang, D. Wang, K. Amine, F. Gao, G. Zhou, S. Thevuthasan, D.R. Baer, J.-G. Zhang, N.D. Browning, J. Liu, C. Wang, Conflicting roles of nickel in controlling cathode performance in lithium ion batteries, Nano Lett. 12 (10) (2012) 5186–5191, https://doi.org/10.1021/nl302249v.

[62] F. Yu, Y. Wang, C. Guo, H. Liu, W. Bao, J. Li, P. Zhang, F. Wang, Spinel LiMn2O4 cathode materials in wide voltage window: single-crystalline versus polycrystalline, Crystals (2022), https://doi.org/10.3390/cryst12030317.

[63] E. Han, Q. Jing, L. Zhu, G. Zhang, S. Ma, The effects of sodium additive on Li1.17Ni0.10Co0.10Mn0.63O2 for lithium ion batteries, J. Alloys Compd. 618 (2015) 629–634, https://doi.org/10.1016/j.jallcom.2014.08.220.

[64] B. Qiu, J. Wang, Y. Xia, Y. Liu, L. Qin, X. Yao, Z. Liu, Effects of Na+ contents on electrochemical properties of Li1.2Ni0.13Co0.13Mn0.54O2 cathode materials, J. Power Sources 240 (2013) 530–535, https://doi.org/10.1016/j.jpowsour.2013.04.047.

[65] E.-S. Lee, K.-W. Nam, E. Hu, A. Manthiram, Influence of cation ordering and lattice distortion on the charge–discharge behavior of LiMn1.5Ni0.5O4 spinel between 5.0 and 2.0 V, Chem. Mater. 24 (18) (2012) 3610–3620, https://doi.org/10.1021/cm3020836.

[66] F. Sigel, B. Schwarz, K. Kleiner, C. Dräger, L. Esmezjan, M. Yavuz, S. Indris, H. Ehrenberg, Thermally induced structural reordering in Li- and Mn-rich layered oxide Li ion cathode materials, Chem. Mater. 32 (3) (2020) 1210–1223, https://doi.org/10.1021/acs.chemmater.9b04355.

[67] G. Assat, D. Foix, C. Delacourt, A. Iadecola, R. Dedryvère, J.-M. Tarascon, Fundamental interplay between anionic/cationic redox governing the kinetics and thermodynamics of lithium-rich cathodes, Nat. Commun. 8 (1) (2017) 2219, https://doi.org/10.1038/s41467-017-02291-9.

[68] W. Choi, H.-C. Shin, J.M. Kim, J.-Y. Choi, W.-S. Yoon, Modeling and applications of electrochemical impedance spectroscopy (EIS) for lithium-ion batteries, J. Electrochem. Sci. Technol. 11 (1) (2020) 1–13, https://doi.org/10.33961/jecst.2019.00528.

[69] D. Wang, T. Xu, Y. Li, D. Pan, X. Lu, Y.-S. Hu, S. Dai, Y. Bai, Integrated surface functionalization of Li-rich cathode materials for Li-ion batteries, ACS Appl. Mater. Interfaces 10 (48) (2018) 41802–41813, https://doi.org/10.1021/acsami.8b16319.

[70] S. Zhao, B. Sun, K. Yan, J. Zhang, C. Wang, G. Wang, Aegis of lithium-rich cathode materials via heterostructured LiAlF4 coating for high-performance lithium-ion batteries, ACS Appl. Mater. Interfaces 10 (39) (2018) 33260–33268, https://doi.org/10.1021/acsami.8b11471.

[71] Y. Su, F. Yuan, L. Chen, Y. Lu, J. Dong, Y. Fang, S. Chen, F. Wu, Enhanced high-temperature performance of Li-rich layered oxide via surface heterophase coating, J. Energy Chem. 51 (2020) 39–47, https://doi.org/10.1016/j.jechem.2020.03.033.

[72] Z. Tai, X. Li, W. Zhu, M. Shi, Y. Xin, S. Guo, Y. Wu, Y. Chen, Y. Liu, Non-stoichiometry of Li-rich cathode material with improved cycling ability for lithium-ion batteries, J. Colloid Interface Sci. 570 (2020) 264–272, https://doi.org/10.1016/j.jcis.2020.03.005.

[73] C. Zhang, Y. Feng, B. Wei, C. Liang, L. Zhou, D.G. Ivey, P. Wang, W. Wei, Heteroepitaxial oxygen-buffering interface enables a highly stable cobalt-free Li-rich layered oxide cathode, Nano Energy 75 (2020), 104995, https://doi.org/10.1016/j.nanoen.2020.104995.

[74] Z. Guo, T. Ma, T. Xu, Y. Chen, G. Yang, Y. Li, Amorphous Li2ZrO3 nanoparticles coating Li[Li0·17Mn0·58Ni0.25]O2 cathode material for enhanced rate and cyclic performance in lithium ion storage, Mater. Chem. Phys. 255 (2020), 123593, https://doi.org/10.1016/j.matchemphys.2020.123593.